Monthly Notices of the ROYAL ASTRONOMICAL SOCIETY

MNRAS **538,** 2396–2407 (2025) https://doi.org/10.1093/mnras/staf435
Advance Access publication 2025 March 17

Neutrino beaming in ultraluminous X-ray pulsars as a result of gravitational lensing by neutron stars

A. A. Mushtukov [1★] A. Y. Potekhin [2,3] I. D. Markozov,[2,3] S. Nallan,[4] K. Kornacka,[5] I. S. Ognev,[6] V. Kravtsov [7] A. A. Dobrynina[6] and A. D. Kaminker [2]

[1]*Astrophysics, Department of Physics, University of Oxford, Denys Wilkinson Building, Keble Road, Oxford OX1 3RH, UK*
[2]*Ioffe Institute, Politekhnicheskaya 26, St Petersburg 194021, Russia*
[3]*Space Research Institute (IKI) of the Russian Academy of Sciences, Profsoyuznaya 84/32, Moscow 117997, Russia*
[4]*Carpe Diem Academy, 6712 Tannahill Drive, San Jose, 95120 CA, USA*
[5]*Christa McAuliffe Academy School of Arts and Sciences, 5200 SW Meadows Rd Ste 150, Lake Oswego, OR 97035, USA*
[6]*P.G. Demidov Yaroslavl State University, Sovietskaya 14, Yaroslavl 150003, Russia*
[7]*Department of Physics and Astronomy, University of Turku, FI-20014 Turku, Finland*

Accepted 2025 March 13. Received 2025 February 12; in original form 2025 January 1

ABSTRACT

X-ray pulsars experiencing extreme mass accretion rates can produce neutrino emission in the MeV energy band. Neutrinos in these systems are emitted in close proximity to the stellar surface and subsequently undergo gravitational bending in the space curved by a neutron star. This process results in the formation of a distinct beam pattern of neutrino emission and gives rise to the phenomenon of neutrino pulsars. The energy flux of neutrinos, when averaged over the neutron star's pulsation period, can differ from the isotropic neutrino energy flux, which impacts the detectability of bright pulsars in neutrinos. We investigate the process of neutrino beam pattern formation, accounting for neutron star transparency to neutrinos and gravitational bending. Based on simulated neutrino beam patterns, we estimate the potential difference between the actual and apparent neutrino luminosity. We show that the apparent luminosity can greatly exceed the actual luminosity, albeit only in a small fraction of cases, depending on the specific equation of state and the mass of the star. For example, the amplification can exceed a factor of 10 for $\approx$0.05 per cent of typical neutron stars with the mass of 1.4 $M_\odot$. Strong amplification is less probable for neutron stars of higher mass. In the case of strange stars, a fraction of high-energy neutrinos can be absorbed, and the beam pattern, as well as the amplification of apparent neutrino luminosity, depends on neutrino energy.

Key words: accretion, accretion discs – stars: neutron – X-rays: binaries.

1 INTRODUCTION

X-ray pulsars (XRPs) are accreting neutron stars (NSs) in close binary systems (see Mushtukov & Tsygankov 2022 for review). Typical field strength at the NS surface here is expected to be $\sim 10^{12}$ G or even stronger. Such a strong magnetic field modifies the geometry of accretion flow directing it towards small regions located close to the poles of an NS and dramatically influences elementary processes of radiation/matter interaction (see Harding & Lai 2006). The luminosity of XRPs is powered by the accretion process, the most efficient mechanism of energy release. The apparent luminosity of XRPs covers about nine orders of magnitude. The lowest detected luminosity is known to be $\sim 10^{32}$ erg s^{-1}. The brightest XRPs show luminosity $\gtrsim 10^{40}$ erg s^{-1} and belong to the class of ultraluminous X-ray sources (ULXs; see Bachetti et al. 2014; Israel et al. 2017; Fabrika et al. 2021 for review).

The geometry of the emission regions at the NS surface is expected to be dependent on the mass accretion rate (Basko & Sunyaev 1975). At a relatively low mass accretion rate ($\lesssim 10^{17}$ g s^{-1}), the accretion flow reaches the stellar surface and is decelerated in the atmosphere of an NS due to the Coulomb collisions, which leads to the formation of hotspots located close to the magnetic poles of a star. At higher mass accretion rates, the luminosity of an NS is sufficiently high ($\gtrsim 10^{37}$ erg s^{-1}) to cause radiative force that stops accretion flow above the stellar surface. It leads to the formation of accretion columns – extended structures confined by a strong magnetic field and supported by the radiation pressure gradient (Wang & Frank 1981; Mushtukov et al. 2015; Zhang, Blaes & Jiang 2022). At mass accretion rates exceeding $\sim 10^{19}$ g s^{-1}, accretion columns can be advective, i.e. X-ray photons are confined inside a sinking region due to large optical thickness of the flow (Mushtukov et al. 2018b). Under this condition, the temperature of plasma can be as high as a few hundred keV, which is sufficient to cause intense creation of electron–positron pairs (Mushtukov, Ognev & Nagirner 2019) and further neutrino emission due to their annihilation (Kaminker et al. 1992). Thus, bright XRPs can manifest themselves as sources of intense neutrino emission, where the total energy flux released due to accretion is channelled into luminosity in photons and luminosity in neutrinos. The intrinsic neutrino luminosity of an NS is maximal right

★ E-mail: alexander.mushtukov@physics.ox.ac.uk

after the supernova explosion and then decreases rapidly with time: it is expected to be $<10^{37}$ erg s^{-1} ($<10^{36}$ erg s^{-1}) after a few $\times\ 10^2$ yr (10^3 yr) after the explosion (Yakovlev et al. 2005), which is well below the expected neutrino luminosity in bright ULXs.

The higher the mass accretion rate and the total luminosity, the larger the fraction of energy released in the form of neutrinos (see fig. 1 in Asthana et al. 2023). The highest accretion rates (and consequently neutrino luminosities) are expected in ULX pulsars and bright Be X-ray transients (Reig 2011) because of their high apparent photon luminosities. However, a high apparent luminosity may not necessarily correspond to a high accretion rate, if radiation is strongly collimated by accretion disc winds, as suggested for these objects by King, Lasota & Kluźniak (2017); see also Lasota & King (2023). On the other hand, this hypothesis is still under debate; the arguments that disfavour strong collimation have been presented e.g. by Mushtukov et al. (2021) and Mushtukov & Portegies Zwart (2023).

Due to the extragalactic nature of confirmed ULX pulsars, the expected neutrino flux is very low and even expected to be significantly below the neutrino isotropic background in a MeV energy band (Asthana et al. 2023). However, estimations of neutrino flux from ULX pulsars (Asthana et al. 2023) were performed under the assumption of isotropic neutrino emission, which can be violated by initial non-isotropic emission as well as by gravitational bending of particle trajectories.

In this paper, we investigate neutrino beam pattern formation accounting for neutrino propagation in a space curved by the gravity of a star and transparency of a star for neutrino emission. The gravitational bending results in a difference between actual (initially generated) L_ν and apparent $L_{\nu,\mathrm{app}}$ neutrino luminosities. The latter can be different for different distant observers. On the basis of calculated beam patterns we obtain expected distributions of neutrino pulsars over the amplification factor:

$$a_\nu \equiv \frac{L_{\nu,\mathrm{app}}}{L_\nu}. \tag{1}$$

2 MODEL SET-UP

2.1 Equation of state and structure of a neutron star

We assume the NS structure to be spherical. Appreciable deviations from the spherical symmetry can be caused by ultrastrong magnetic fields ($B \gtrsim 10^{17}$ G) or by rotation with ultrashort periods (less than a few milliseconds; see e.g. Haensel, Potekhin & Yakovlev 2007 and references therein), but we will not consider such cases.

The general static isotropic metric satisfying the Einstein field equations can be written in the 'standard form' using the Schwarzschild coordinates as follows [see e.g. section 8.1 in Weinberg (1972) and section 23 in Misner, Thorne & Wheeler (1973)]:

$$\mathrm{d}s^2 = -B(r)\,\mathrm{d}t^2 + A(r)\,\mathrm{d}r^2 + r^2(\mathrm{d}\theta^2 + \sin^2\theta\,\mathrm{d}\phi^2), \tag{2}$$

where t is the time coordinate, r, θ, and ϕ are the spherical polar coordinates,

$$A(r) = \left(1 - \frac{2GM_r}{c^2 r}\right)^{-1}, \quad B(r) = \mathrm{e}^{2\Phi/c^2}, \tag{3}$$

M_r is the gravitational mass inside a sphere of radius r, G is the Newtonian constant of gravitation, Φ is the gravitational potential, and c is the speed of light in a vacuum. Then the mechanical structure of an NS is governed by four first-order differential equations for r, M_r, Φ, and the local pressure P as functions of baryon number β inside a given spherical shell (e.g. Richardson, van Horn & Savedoff 1979):

$$\frac{\mathrm{d}r}{\mathrm{d}\beta} = \frac{1}{4\pi r^2 \bar{n}\sqrt{A(r)}}, \tag{4}$$

$$\frac{\mathrm{d}M_r}{\mathrm{d}\beta} = \frac{\rho}{\bar{n}\sqrt{A(r)}}, \tag{5}$$

$$\frac{\mathrm{d}\Phi}{\mathrm{d}\beta} = G\,\frac{M_r + 4\pi r^3 P/c^2}{4\pi r^4 \bar{n}}\,\sqrt{A(r)}, \tag{6}$$

$$\frac{\mathrm{d}P}{\mathrm{d}\beta} = -\left(\rho + \frac{P}{c^2}\right)\frac{\mathrm{d}\Phi}{\mathrm{d}\beta}, \tag{7}$$

where $\bar{n}$ is the mean number density of baryons. We integrate these equations from $r = 0$ and $M_r = 0$ at the centre of the star outwards, starting from a predefined baryon density $\bar{n}$ at the centre, until a predefined mass density at the outer boundary ρ_b is reached.

The boundary condition for the gravitational potential Φ is provided by the Schwarzschild metric outside the star,

$$\mathrm{e}^{2\Phi_\mathrm{b}/c^2} = 1 - \frac{2GM}{Rc^2}, \tag{8}$$

where R and $M = M_R$ are the stellar radius and mass, and Φ_b is the value of Φ at the stellar surface. Since the value of Φ at the centre of the NS is not known in advance, we integrate equation (6) for a shifted potential $\tilde{\Phi}(\beta) = \Phi(\beta) - \Phi(0)$, with the initial value $\tilde{\Phi}(0) = 0$ at the centre of the star, and the value of the shift $\Phi(0)$ is found from equation (8) after the integration has been completed.

We solve the set of equations (4)–(7) numerically by the classic Runge–Kutta method on a non-uniform grid in β, with variable steps adapted to provide sufficient accuracy at each grid node for each of the computed functions. We decrease each step until the desired accuracy is reached. In order to prevent accuracy loss in the outer layers of the star, where β is nearly constant as a function of ρ or r, we use the difference $(\beta_\mathrm{b} - \beta)$ as an independent variable, β_b being the value of β at $r = R$, which is equal to the total number of baryons in the NS.

We limit ourselves to three equations of state (EoSs): APR (Akmal, Pandharipande & Ravenhall 1998), SLy4 (Douchin & Haensel 2001), and BSk24 (Pearson et al. 2018). These EoSs describe the ground state for the nucleon–lepton ($npe\mu$) composition of matter, which is the most conservative assumption, without any 'exotic' constituents. The APR EoS for the NS core is based on realistic effective two- and three-nucleon interactions, which allow one to reproduce various nucleon scattering data and the properties of light nuclei. We adopt the version of the APR EoS named A18 + δv + UIX* in Akmal et al. (1998), which includes a relativistic boost correction, in the parametrized form of Potekhin & Chabrier (2018). This parametrization includes the NS crust described by the BSk24 EoS on top of the core described by the APR EoS. The SLy and BSk models are based on effective nucleon–nucleon interactions of the Skyrme type, adjusted to reproduce the EoS of pure neutron matter and the experimental properties of heavy atomic nuclei. These EoS models are *unified*: they are based on the same microscopic models for the core and the crust. For the first (SLy) EoS family, we use the SLy4 EoS in the parametrized form of Haensel & Potekhin (2004). The more recent BSk interaction model is more complicated; it is better tuned to the recent collection of experimental nuclear data. The BSk24 and BSk25 versions of this model, which are very similar, appear to be preferred, as discussed by Pearson et al. (2018). The BSk24 EoS is substantially stiffer than the SLy4 EoS, and we choose it as a representative example of relatively stiff and soft EoS models.

We also consider the possibility of the EoS of strange matter built of the u, d, and s quarks (Witten 1984; Alcock, Farhi & Olinto

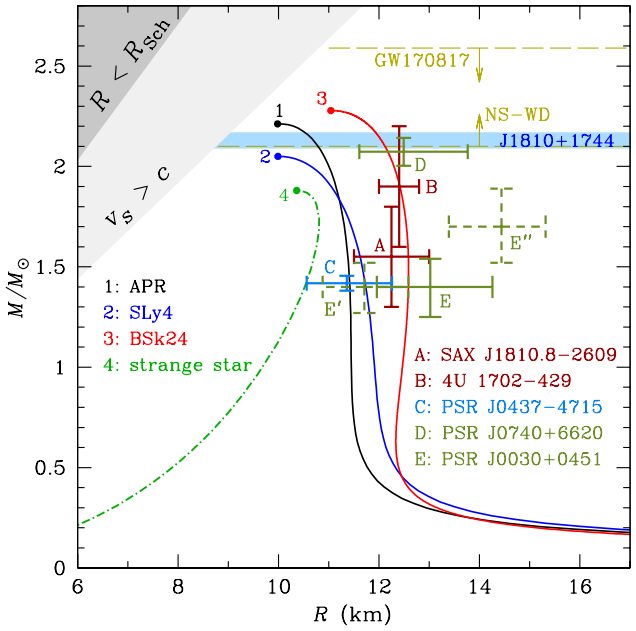

Figure 1. NS mass M versus radius R for four EoS models compared with theoretical and observational constraints and estimates. The solid curves labelled with numbers 1–3 show mass–radius relations for APR (1), SLy4 (2), and BSk24 (3) EoS models, respectively. The dashed–dotted line shows an example of mass–radius relation for a strange star. The curves are truncated at the hydrostatic stability limits, marked by the heavy dots. The dark and light grey shaded triangles are prohibited by general relativity and causality. The horizontal light-blue band corresponds to the mass estimate (with 1σ uncertainties) for PSR J1810+1744. The horizontal dashed lines with arrows mark the upper and lower 3σ limits to the maximum NS mass, derived from observations. The error bars show the 1σ confidence intervals in M and R, inferred from observations of five NSs in binary systems, marked by the letters from A to E, according to the legend (see text for details).

1986; Haensel, Zdunik & Schaefer 1986). For the strange matter EoS, we use the approximation proposed by Zdunik (2000) and adopt the fiducial parameters in their paper: the bag constant $B = 60\,\mathrm{MeV\,fm^{-3}}$, the QCD coupling constant $\alpha_\mathrm{c} = 0$, and the rest energy of the strange quark $m_\mathrm{s}c^2 = 100$ MeV.

The solid curves in Fig. 1 show gravitational mass M versus circumferential radius R of an NS for the three selected EoSs. The dot–dashed curve displays $M(R)$ for a strange star model. The dark grey shaded area ($R < R_\mathrm{Sch}$, where $R_\mathrm{Sch} = 2GM/c^2$ is the Schwarzschild radius) is prohibited by general relativity. The entire grey-shaded triangle is prohibited by general relativity combined with the condition that the speed of sound must be subluminal (e.g. section 6.5.7 of Haensel et al. 2007).

The lower horizontal dashed line with the upward arrow marks the lower 3σ limit to the maximum NS mass, $M_\mathrm{max} > 2.09$, obtained by Romani et al. (2022) jointly for seven most massive known NSs in binaries with white dwarfs (WDs). The light-blue horizontal band corresponds to the most accurate of individual estimates for these NSs ($M = 2.13 \pm 0.04\,\mathrm{M_\odot}$ for PSR J1810+1744). These mass estimates rely on an analysis of orbital light curves with a specific model for heating of the WD surface by radiation from a pulsar, hence they can be model dependent. Pulsar mass estimates were obtained using the effects of general relativity (in particular the Shapiro delay of the pulsar signal) appear to be less model dependent. However, one of the largest estimates of this kind ($M = 2.01 \pm 0.04\,\mathrm{M_\odot}$ for PSR J0348+0432; Antoniadis et al. 2013) was recently revised to a 10 per cent lower value ($M = 1.806 \pm 0.037\,\mathrm{M_\odot}$; Saffer et al. 2024). The highest reliable pulsar mass estimates, based on the Shapiro delay measurements, are currently $M = 2.073 \pm 0.069\,\mathrm{M_\odot}$ with the lower bound $M > 1.95\,\mathrm{M_\odot}$ at the 95.4 per cent confidence level for PSR J0740+6620 (Fonseca et al. 2021) and $M = 1.908 \pm 0.016\,\mathrm{M_\odot}$ for PSR J1614−2230 (Arzoumanian et al. 2018).

Rezzolla, Most & Weih (2018) used quasi-universal relations exhibited by equilibrium solutions of rotating relativistic stars to infer constraints on the maximum NS mass from an analysis of the electromagnetic and gravitational wave signals from the double NS merger GW170817. Their most conservative upper limit $M_\mathrm{max} < 2.59\,\mathrm{M_\odot}$ is shown in Fig. 1 by the upper horizontal dashed line with the downward arrow. It relies on the assumption that the merger product in GW170817 has collapsed into a black hole. However, the kilonova produced in this event could also be explained in an alternative scenario of NS stripping without black hole formation (Blinnikov et al. 2022). Thus the indicated limit is model dependent.

The vertical and horizontal error bars in Fig. 1 show the available 1σ confidence intervals in M and R, respectively, for the cases where these uncertainties are not large ($\lesssim$15 per cent). The labels A and B mark such intervals for the bursters SAX J1810.8−2609 and 4U 1702−429, according to the analysis by Nättilä et al. (2017). The label C corresponds to the nearest and brightest millisecond pulsar PSR J0437−4715 in an NS–WD binary system, according to Choudhury et al. (2024). Labels D and E mark the results obtained for PSR J0740+6620 (Salmi et al. 2024) and PSR J0030+0451 (Miller et al. 2019), respectively, using an analysis of the energy-dependent thermal X-ray waveform observed by the *Neutron Star Interior Composition Explorer* (*NICER*). Despite the belief that this approach was 'less subject to systematic errors than other approaches for estimating neutron star radii' (Miller et al. 2019), a subsequent reanalysis, performed for PSR J0030+0451 by Vinciguerra et al. (2024) with alternative hotspot models and using jointly the data of *NICER* and *XMM–Newton*, resulted in substantially different estimates, shown in Fig. 1 by the dashed error bars and marked as E′ and E″, which demonstrate the strong model dependence. Other joint mass and radius estimates obtained from spectral analyses of X-ray radiation of NSs exhibit similar model dependence and are not plotted here (e.g. Tanashkin et al. 2022; see also discussion and references in Potekhin et al. 2020).

Fig. 1 demonstrates that the selected EoS models are reasonably compatible with the available observational NS mass and radius estimates, although the softest SLy4 EoS is only marginally compatible with the lower limits to M_max.

Solutions of the stellar structure equations for the three selected NS EoSs are illustrated in Fig. 2. The upper and lower panels show, respectively, mass density ρ and gravitational mass distributions M_r as functions of r for the total mass of an NS equal to $1.4\,\mathrm{M_\odot}$ (left panels) or $2\,\mathrm{M_\odot}$ (right panels). The dot–dashed line in the left panels shows analogous distributions for the model of a strange star with $M = 1.4\,\mathrm{M_\odot}$.

2.2 Neutrino emission and propagation

2.2.1 Neutrino opacities

The distinct feature of neutrino propagation near an NS stems from the fact that NSs are typically transparent to neutrino emissions of relatively low energy (Sawyer & Soni 1979; Haensel & Jerzak 1987), unless their internal temperature T exceeds $\sim 10^{10}$ K ($k_\mathrm{B}T \sim 1$ MeV, where k_B is the Boltzmann constant), which occurs only immediately following a supernova explosion (see e.g. figs 3 and 9 in Potekhin &

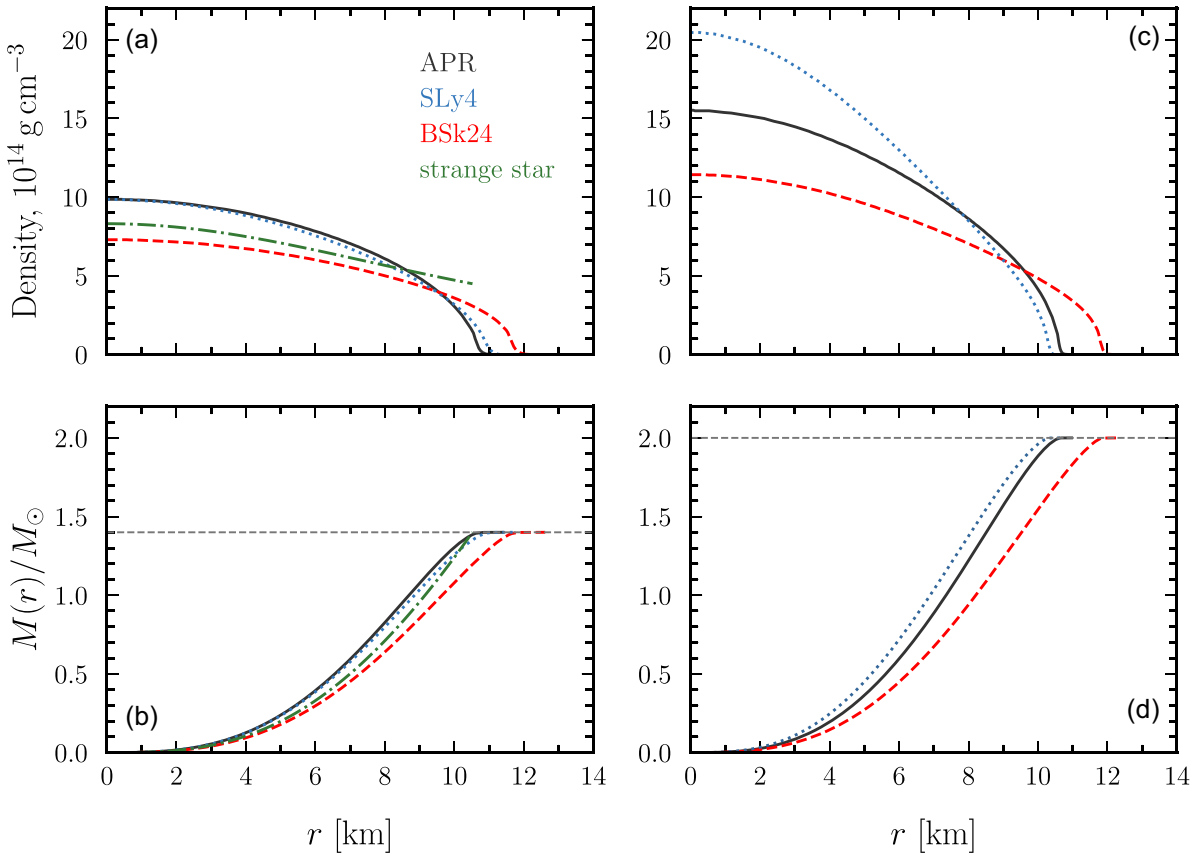

Figure 2. Mass density (panels a and c) and mass (panels b and d) distributions inside an NS/strange star of a given total mass and EoS. Different curves are calculated for different EoS: APR (black solid), SLy4 (blue dotted), BSk24 (red dashed), and EoS for a strange star according to Zdunik (2000). Mass of an NS is fixed at $M = 1.4\,\mathrm{M}_\odot$ in panels (a) and (b), and at $M = 2\,\mathrm{M}_\odot$ in panels (c) and (d). The mass of a strange star was taken to be $M = 1.4\,\mathrm{M}_\odot$ in panel (a).

Chabrier 2018). In bright XRPs, it is expected that neutrinos are emitted near the base of the accretion column. We assume that the magnetic field near the NS surface is dominated by the dipole component, leading to neutrinos being initially emitted near the magnetic poles of the NS located diametrically opposite on the stellar surface.[1] The primary process of neutrino production involves the annihilation of electron–positron pairs, although a fraction of neutrinos can also be generated via the synchrotron process (see e.g. Kaminker et al. 1992; Mushtukov et al., in preparation). Emitted neutrinos propagate both outside and inside the NS, which is cold enough to be nearly transparent to them. All emitted neutrinos undergo gravitational bending in curved space–time. Neutrino emission and their subsequent propagation along curved trajectories form a distinct beam pattern. While the vast majority of neutrinos initially emitted at the NS surface are of electron flavour, the composition of the neutrino flux varies as it propagates, because of neutrino oscillations. Neutrinos of very high energies E_ν (above several MeV; see below) may experience scatterings in the core of the NS, which influence their trajectories and, consequently, their final angular distribution, but we will not consider such high energies here.

[1]Note that in a few XRPs, non-dipole magnetic field structures have been proposed to explain observational data (see e.g. Postnov et al. 2013; Israel et al. 2017; Tsygankov et al. 2017; Mönkkönen et al. 2022).

The primary processes governing neutrino opacity in dense matter are neutrino–neutron scattering (see e.g. Shapiro & Teukolsky 1983),

$$n + \nu_{\mathrm{e},\mu} \longrightarrow n + \nu_{\mathrm{e},\mu}, \tag{9}$$

and neutrino absorption,

$$n + \nu_{\mathrm{e}} \longrightarrow p + e^-, \qquad n + \nu_\mu \longrightarrow p + \mu^-. \tag{10}$$

The neutrino mean free path in the elastic limit of neutrino–neutron scattering (9) for non-degenerate nucleons can be estimated as (e.g. equation 11.7.8 in Shapiro & Teukolsky 1983)

$$\bar{\lambda}_{\mathrm{sc},0} \sim 3\,\frac{\rho_{\mathrm{nuc}}}{\rho}\left(\frac{1\,\mathrm{MeV}}{E_\nu}\right)^2\ \mathrm{km}, \tag{11}$$

where $\rho_{\mathrm{nuc}} \approx 2.5 \times 10^{14}\,\mathrm{g\,cm^{-3}}$ denotes the mass density at the saturation number density of baryons $n_{\mathrm{nuc}} \approx 0.15\ \mathrm{fm^{-3}}$ (Horowitz, Piekarewicz & Reed 2020).

However, at temperatures $T \lesssim 10^8$ K and densities $\rho \sim (1\text{–}5)\rho_{\mathrm{nuc}}$, typical for mature NSs (unlike, for instance, non-degenerate regions of a proto-NS), the neutrino energies most relevant for the ULXs ($E_\nu \sim 0.1$–1 MeV) are large compared with temperature T but small compared with neutron Fermi energy E_{Fn}. Under these conditions, the mean free path $\bar{\lambda}_{\mathrm{sc}}$ increases compared with $\bar{\lambda}_{\mathrm{sc},0}$ by a factor $\propto E_{\mathrm{Fn}}/E_\nu$ (see e.g. equation 7.2 in Iwamoto 1982). Then the neutrino mean free path $\bar{\lambda}_{\mathrm{sc}}$ in the elastic limit of neutrino–neutron scattering (equation 9) can be estimated from equation (26) in Sawyer & Soni

(1979) or (similar assessment) equation (7.2) in Iwamoto (1982),

$$\bar{\lambda}_{\rm sc} \approx 800 \left(\frac{n_{\rm nuc}}{n_{\rm n}}\right)^{2/3} \left(\frac{1\,{\rm MeV}}{E_\nu}\right)^3 {\rm km}, \tag{12}$$

where $n_{\rm n}$ is the number density of neutrons, so that $\bar{\lambda}_{\rm sc} \gg R$.

The neutrino absorption process (equation 10) is forbidden in the degenerate NS matter at $p_{\rm Fn} \gg p_{\rm Fp} + p_{\rm Fe}$ (for the same reason as the direct Urca process; cf. e.g. section 11.2 in Shapiro & Teukolsky 1983), where $p_{\rm F(n,p,e)}$ are the Fermi momenta of neutrons, protons, and electrons, respectively. Thus in the bulk of a typical NS, absorption of neutrinos proceeds (in analogy with the modified Urca processes) via the modified reactions:

$$n + n + \nu_{\rm e} \longrightarrow p + n + e^-, \quad n + p + \nu_{\rm e} \longrightarrow p + p + e^-, \tag{13}$$

with the mean free paths $\bar{\lambda}_{\rm abs}$ still longer than $\bar{\lambda}_{\rm sc}$ at the low temperatures (Sawyer & Soni 1979; Iwamoto 1982; Haensel & Jerzak 1987). In this case, $\bar{\lambda}_{\rm abs}$ is given by equation (16) in Sawyer & Soni (1979) or equation (20) in Haensel & Jerzak (1987). At the nuclear saturation density, we can estimate $\bar{\lambda}_{\rm abs}$ using the convenient formula (equation 22) in Sawyer & Soni (1979), which agrees with fig. 1 in Haensel & Jerzak (1987) at $T = 5 \times 10^{10}$ K and reproduces the scaling law (equation 25) in Haensel & Jerzak (1987). At the densities and temperatures typical for the core of a mature NS, $\bar{\lambda}_{\rm abs}$ increases with decreasing energy E_ν from $\bar{\lambda}_{\rm abs} \sim$ (1–3) $\times 10^6$ km at $E_\nu = 1$ MeV to $\bar{\lambda}_{\rm abs} \sim$ (1–3) $\times 10^{10}$ km at $E_\nu = 0.1$ MeV.

In the quark (degenerate) matter, in contrast to the nucleon matter, neutrino scattering is less efficient than absorption by quarks (e.g. Pal & Dutt-Mazumder 2011), because the processes similar to equation (10), e.g. $d + \nu_{\rm e} \to u + e^-$, are allowed (see e.g. Iwamoto 1982). In this case, we have $\bar{\lambda}_{\rm qabs}/\bar{\lambda}_{\rm qsc} \ll 1$, where $\bar{\lambda}_{\rm qabs}$ and $\bar{\lambda}_{\rm qsc}$ are electron neutrino mean free paths due to absorption and scattering in quark matter, respectively.

The absorption coefficient of non-degenerate neutrinos in the quark matter can be assessed with equation (30) by Pal & Dutt-Mazumder (2011). Let us assume $E_\nu \gg \pi k_{\rm B} T$, adopt the standard quark colour factor $C_{\rm F} = 4/3$ and neglect higher order corrections in this equation, retaining only the leading term, which is equivalent to equation (6.8) of Iwamoto (1982). Then we have

$$\bar{\lambda}_{\rm qabs} \approx \frac{14\,{\rm km}}{\alpha_{\rm s}\mu_{\rm u,500}\mu_{\rm d,500}\mu_{\rm e,11}} \left(\frac{1\,{\rm MeV}}{E_\nu}\right)^2, \tag{14}$$

where $\alpha_{\rm s}$ is the strong coupling constant, $\mu_{\rm u,500} = \mu_{\rm u}/(500\,{\rm MeV})$, $\mu_{\rm d,500} = \mu_{\rm d}/(500\,{\rm MeV})$, $\mu_{\rm e,11} = \mu_{\rm e}/(11\,{\rm MeV})$, $\mu_{\rm u,d,e}$ being the chemical potentials of the u and d quarks and of the electrons. For estimates, following Schäfer & Schwenzer (2004) and Pal & Dutt-Mazumder (2011), we set $\alpha_{\rm s} = \mu_{\rm u,500} = \mu_{\rm d,500} = \mu_{\rm e,11} = 1$, which corresponds to densities $\rho \approx 6\rho_{\rm nuc}$.

2.2.2 *Neutrino trajectories*

To characterize the geometry of space–time around an NS, we employ the static spherically symmetric metric in the standard form, equation (2). It is a suitable approximation for NSs in XRPs with typical spin periods $P_{\rm spin} \gtrsim 0.1$ s (see e.g. Haensel et al. 2007). For a spherically symmetric NS in hydrostatic equilibrium, metric (equation 2) is locally similar to the Schwarzschild metric produced by mass M_r. In this metric, each trajectory of a freely propagating neutrino lies in one and the same plane. Within this plane, we parametrize the trajectory using polar coordinates, with $r \geq 0$ and $\varphi \in [0, 2\pi]$. Since the neutrino rest masses are negligibly small compared with the considered neutrino energies, we describe a neutrino trajectory by an equation for a particle with zero rest mass.

The derivation of the general equations of motion in metric (equation 2) can be found, e.g. in Weinberg (1972). In particular, a trajectory of a particle in the equatorial plane (i.e. with the polar coordinate $\theta = \pi/2$) is given by equation (8.4.29) of Weinberg (1972). For a massless particle, we should set the right-hand side of this equation to zero, which leads to

$$\frac{A(r)}{r^4}\left(\frac{{\rm d}r}{{\rm d}\varphi}\right)^2 + \frac{1}{r^2} = \frac{1}{B(r)b^2}, \tag{15}$$

where $A(r)$ and $B(r)$ are determined by equation (3), and b has the physical meaning of the impact parameter, which is constant along every given trajectory due to the angular momentum conservation. For each trajectory, b is determined by the initial neutrino direction. At the NS surface, it is related to the angle ζ between the radial direction and neutrino trajectory as (see Appendix A)

$$b = \frac{R\sin\zeta}{\sqrt{1 - R_{\rm Sch}/R}}, \tag{16}$$

where $R_{\rm Sch} = 2GM/c^2$ is the Schwarzschild radius.

In the empty space outside an NS (at $r > R$), $A(r)B(r) = 1$ (see e.g. Weinberg 1972, section 8.2). In this case, equation (15) reduces to equation (25.55) in Misner et al. (1973), which describes a photon trajectory in the Schwarzschild metric. Inside an NS (at $r < R$), the functions $A(r)$ and $B(r)$ are determined by the EoS through the solution of the hydrostatic equilibrium equations (4)–(7). Consequently, trajectories of neutrinos propagating through an NS are contingent upon the mass distribution within the star and are thus anticipated to vary for different EoSs.

2.3 Neutron star rotation and luminosity distribution

The apparent luminosity of an NS can be determined as

$$L_{\nu,{\rm app}} = \frac{4\pi D^2}{t_{\rm av}} \int_0^{t_{\rm av}} F_\nu(t)\,{\rm d}t, \tag{17}$$

where $F_\nu(t)$ is variable neutrino energy flux density (as registered by a distant observer), which varies with time t, D is a distance to the compact object, and $t_{\rm av}$ is a time interval for the averaging. In practice, the integration in equation (17) is performed over a long time interval ($t_{\rm av} \gg P_{\rm spin}$) because the mass accretion rate in X-ray binaries is known to fluctuate over a wide range of time-scales, which should result in fluctuating pulse profiles in X-rays and neutrinos. The ratio of the apparent and actual neutrino luminosity determines the neutrino amplification factor a_ν, equation (1).

Apparent neutrino luminosity depends on actual neutrino luminosity, neutrino beam pattern, and geometry of NS rotation in the observer's reference frame. Rotation of an NS in the observer's reference frame is described by two angles: inclination i (i.e. the angle between the rotation axis and observer's line of sight) and the magnetic obliquity θ_B (i.e. the angle between the rotational and magnetic axis of an NS). The flux is related to the neutrino flux distribution in the reference frame of an NS, which depends on the angle ψ between the observer's line of sight and NS magnetic axis at a given phase $\varphi_{\rm p} \in [0; 2\pi]$ of NS rotation:

$$\cos\psi = \cos i\cos\theta_B + \sin i\sin\theta_B\cos\varphi_{\rm p}. \tag{18}$$

The angles i and θ_B are typically unknown for the XRPs. Recent observation of X-ray polarization variable over NS spin period, however, sheds light on rotation geometry in some particular accreting strongly magnetized NSs (Doroshenko et al. 2022, 2023;

Tsygankov et al. 2022, 2023; Heyl et al. 2024; Malacaria et al. 2023; Mushtukov et al. 2023; Forsblom et al. 2024), but features of NS distribution over rotation parameters are still uncertain. To estimate possible deviations of apparent neutrino luminosity from the actual one, we assume a random distribution of NSs over the angles i and θ_B, simulate neutrino pulse profiles for various i and θ_B, and calculate theoretical distributions $f(a_\nu)$ of NSs over the apparent neutrino luminosity amplification factors a_ν. The technique used here is similar to the one applied to investigate distributions of XRPs over the apparent luminosity in X-rays (see e.g. Mushtukov et al. 2021; Markozov & Mushtukov 2024).

3 NUMERICAL MODEL

Our numerical procedure consists of two stages. First, we compute the angular distribution of neutrino flux in the reference frame of an NS accounting for neutrino propagation along curved trajectories and absorption inside a star. Then, using the computed angular distribution, we simulate neutrino flux variability in the observer's reference frame due to the rotation of an NS and calculate the theoretical distribution of neutrino pulsars over the neutrino amplification factor.

3.1 Neutrino angular distribution

To obtain the angular distribution of neutrinos, we specify neutrino energy E_ν, NS EoS, and mass, which give us NS radius and internal mass distribution. Then we perform Monte Carlo simulations to calculate trajectories of 4×10^7 particles in each run.

As an example, we consider the case when neutrino absorption is much more efficient than scattering, so scattering can be neglected. Then the simulation includes the following steps:

(i) We start with the neutrino of energy E_ν emitted from the surface of an NS near one of its magnetic poles. The initial direction of particle motion is taken to be random and calculated under the assumption that the initial angular distribution of neutrinos is isotropic.

(ii) We choose a random realization of the optical depth travelled by the particle before its absorption (the dimensionless free path) according to the formula $\tau_X = -\ln X,$, where $X \in (0; 1)$ is a random number having a uniform distribution.

(iii) We simulate a particle trajectory by numerically solving the differential equation (15) for a set of initial parameters, where the initial impact factors are calculated according to equation (16) (see Appendix B). If the trajectory crosses the star, we calculate the optical depth travelled by the particle, τ_ν, by integrating along the simulated trajectory,

$$\tau_\nu(s) = \int_0^s \frac{\mathrm{d}s'}{\bar{\lambda}(s')}, \tag{19}$$

where s is the path-length along the particle trajectory. The mean free path $\bar{\lambda}$ is given by

$$\bar{\lambda} = \frac{1}{\bar{\lambda}_{\rm abs}^{-1} + \bar{\lambda}_{\rm sc}^{-1}} \simeq \bar{\lambda}_{\rm abs}, \tag{20}$$

which accounts for both absorption ($\bar{\lambda}_{\rm abs}$) and scattering ($\bar{\lambda}_{\rm sc}$). These quantities depend on the neutrino energy E_ν, which experiences gravitational redshift (equation A11) while the particle moves along its trajectory, and the mass density ρ at each point along the path inside the star, according to the estimates in Section 2.2. The length element $\mathrm{d}s'$ in equation (19) is calculated using equation (A10) in Appendix A.

The optical depth (equation 19) is a non-decreasing function, bounded from above by some maximum value for every simulated trajectory. If τ_X exceeds this maximum, the particle goes to infinity without absorption and we account for its final momentum direction in the simulated angular distribution function. Then we return to step (i) and start the simulation for the next particle. Otherwise, $\tau_\nu(s)$ reaches τ_X at some point in the trajectory. In this case, the particle is considered to be absorbed, we drop it from further consideration, return to step (i) and start the simulation for the next neutrino. Thus simulating trajectories of a large number of particles, we arrive at the final angular distribution of neutrinos in the NS reference frame.

The described algorithm is rather general. However, as argued in Section 2.2.1, the scattering and absorption do not noticeably affect neutrino flux and can be neglected in a cold NS at the energies considered in this study. On the other side, the neutrino absorption can play a noticeable role in a strange quark star, as will be seen below in Fig. 7.

3.2 Neutrino amplification factor

To get the amplification factor (equation 1) for given rotation parameters i and θ_B, we use pre-calculated neutrino flux distribution in the reference frame of a star (Section 3.1) and apply equation (21) to compute the theoretical pulse profile in neutrino emission. The variation of the angle ψ between the line of sight and the magnetic field axis is given by

$$\cos\psi = \sin i \sin\theta_B \cos\varphi_{\rm p} + \cos i \cos\theta_B, \tag{21}$$

where i is the inclination angle of the observer's line of sight with respect to the rotational axis, and θ_B is the angle between the magnetic field axis and the rotational axis. The phase angle of pulsations, $\varphi_{\rm p} \in [0, 2\pi)$, represents the rotational phase of the NS, with $\varphi_{\rm p} = 0$ corresponding to a reference position in the star's rotation. Calculating the theoretical pulse profile, we assume that neutrinos are emitted from two magnetic poles of an NS which are positioned on opposite sides of the stellar surface. In our simulations, the mass accretion rate is assumed to be constant. Under this condition, the pulse profile does not experience variations from one pulse period to another, and we use $t_{\rm av} = P_{\rm spin}$ in equation (17). Averaging the neutrino flux variable over the NS spin period, we obtain the apparent neutrino luminosity (equation 17). Dividing it by the actual neutrino luminosity L_ν, defined as the initial neutrino flux integrated over the emission region as seen by a distant observer (i.e. corrected for the gravitational redshift), we obtain the neutrino amplification factor (equation 1) for any given rotation geometry, mass, EoS of the star, and emitted neutrino energy.

To obtain the theoretical distribution of neutrino pulsars over the amplification factors $f(a_\nu)$ we perform Monte Carlo simulations. In each simulation, we construct a neutrino pulse profile and calculate apparent neutrino luminosity for NS inclination,

$$i = \arccos(1 - 2X_1), \tag{22}$$

and magnetic obliquity,

$$\theta_B = \pi X_2, \tag{23}$$

where $X_1,\ X_2 \in (0; 1)$ are random numbers. The constructed differential distribution function $f(a_\nu)$ is normalized as

$$\int_0^\infty f(a_\nu)\,\mathrm{d}a_\nu = 1. \tag{24}$$

In practice, it is useful to consider the cumulative distribution function describing the fraction of objects amplified by a factor larger

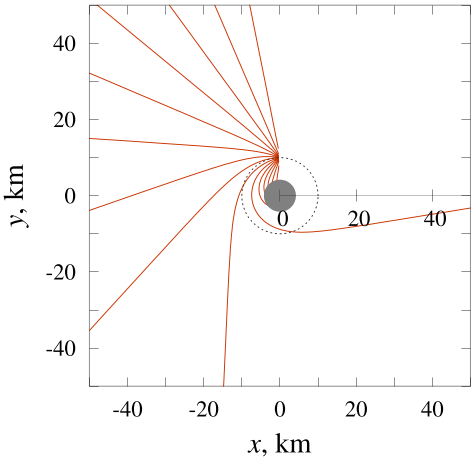

Figure 3. Examples of neutrino trajectories calculated for particles emitted at the distance 10^6 cm from the Schwarzschild black hole with mass $M = 1.4\,\mathrm{M}_\odot$. The grey circular area is the region surrounded by the Schwarzschild radius $R_{\rm Sch}$, while the blue dotted circle marks the distance $r = 10$ km from the centre.

than a_ν:

$$\mathcal{F}(a_\nu) \equiv \int_{a_\nu}^{\infty} f(x)\,\mathrm{d}x. \tag{25}$$

4 NUMERICAL RESULTS

In this section, we demonstrate the results of our numerical simulations of neutrino trajectories (Section 4.1), the angular distribution of neutrino energy flux (Section 4.2), and theoretical distributions of neutrino pulsars over the neutrino amplification factor (Section 4.3). The gravitational bending of neutrinos propagating through a star is affected by the internal mass distribution. We analyse mass density distributions calculated for three specific NS EoSs (see Section 2.1), assuming NS masses of 1.4 and $2\,\mathrm{M}_\odot$, and for a strange star, assuming its mass of $1.4\,\mathrm{M}_\odot$. In the latter case, to demonstrate the possible impact of neutrino absorption in a compact star, we perform simulations for neutrinos of different energies.

4.1 Neutrino trajectories

Examples of neutrino trajectories calculated in the Schwarzschild metric near a $1.4\,\mathrm{M}_\odot$ black hole are shown in Fig. 3. Fig. 4 depicts neutrino trajectories emitted from the surface of $1.4\,\mathrm{M}_\odot$ (upper panel) and $2\,\mathrm{M}_\odot$ (lower panel) NS. Unlike photons, neutrinos can penetrate into a compact star, where their trajectories follow geodesic paths. Within the star, neutrino trajectories are influenced by the mass distribution, gravitational potential, and pressure (see Appendix A for details). The greater the mass of a star and the more concentrated its matter is toward the centre, the larger the deviation of particles from their original propagation direction, i.e. the deflection angle (see Fig. 5).

4.2 Angular distribution of neutrino flux

Utilizing the calculated neutrino trajectories, we derive the angular distribution of neutrino energy flux in the reference frame of an NS (i.e. in a frame where the star does not rotate). Neutrino trajectories started from the magnetic pole at the NS surface are curved and tend

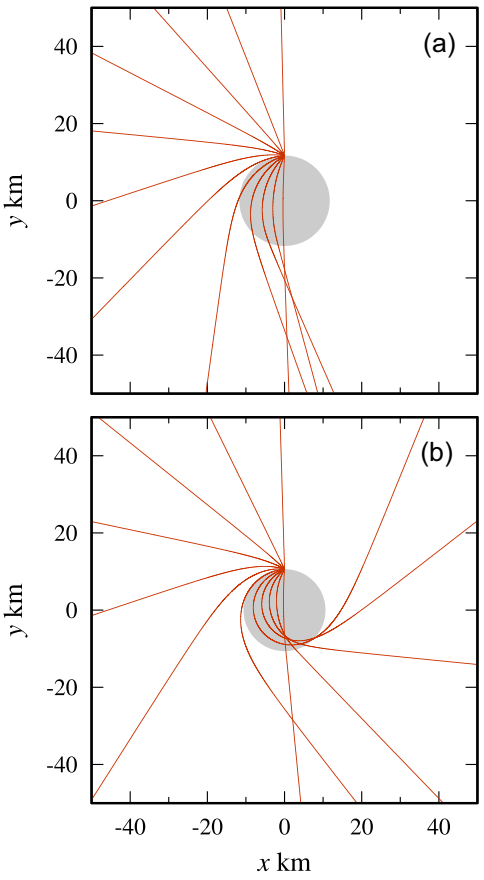

Figure 4. Examples of neutrino trajectories calculated for particles emitted at the NS surface for the case of different NS mass (and radius): (a) $M = 1.4\,\mathrm{M}_\odot$ and (b) $M = 2\,\mathrm{M}_\odot$. In these calculations, the SLy4 EoS is assumed. For comparison, the same uneven steps for the initial colatitudes of trajectories are chosen in both panels.

to converge in certain directions, leading to a significant amplification of the neutrino energy flux in those areas. The directions of enhanced flux depend on the NS mass and internal structure, which are governed by the EoS. We note that the angular distributions of neutrino flux always show two peaks. The first peak is in the direction opposite to the magnetic pole of a star that produces neutrinos, i.e. at colatitude $\sim\pi$ (see Fig. 6). Similar peaks have been reported earlier for photons lensed in the gravitational field of an NS (see figs 3, 4, and 9 in Riffert & Meszaros 1988; figs 8 and 9 in Kraus 2001; figs 10–12 in Mushtukov et al. 2018a; and fig. 6 in Mushtukov et al. 2024). The second peak in the angular distribution corresponds to neutrinos experiencing the maximal deflection $\Delta\zeta$ (see Fig. 5), at colatitude $\sim[2\pi - (\zeta + \Delta\zeta)]$ (see Fig. 6). The angular distribution of neutrinos depends on both the EoS (compare different panels in Fig. 6) and the mass of an NS (compare solid red and dotted black lines in Fig. 6). For NSs with smaller masses, the maximum enhancement of the neutrino flux is more pronounced. In contrast, more massive NSs deflect neutrinos more strongly from their original propagation direction. It results in an angular distribution that is closer to the isotropic one, albeit with distinct peaks still present.

In the case of strange stars, unlike the NSs, neutrino absorption can be noticeable. Nevertheless, angular distribution becomes strongly anisotropic and neutrino energy flux can exceed the isotropic flux by

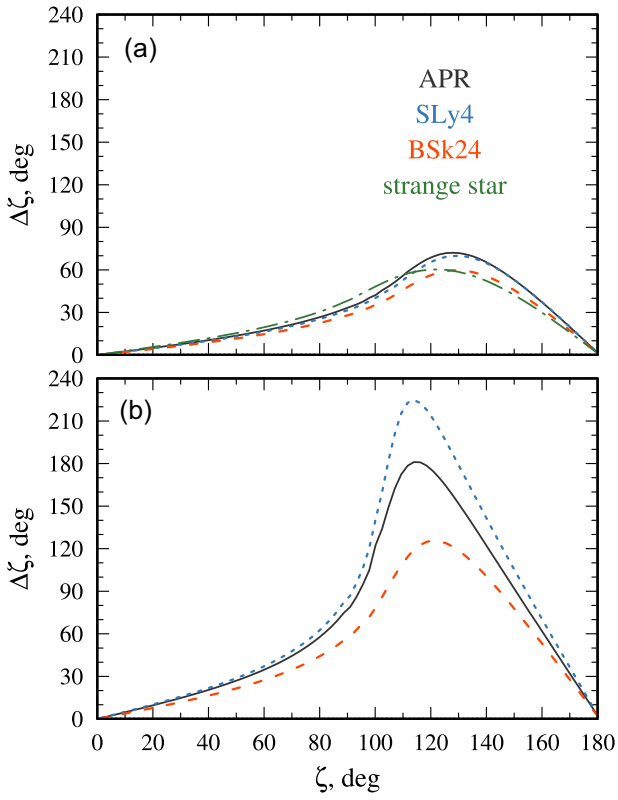

Figure 5. The deflection angle for neutrinos emitted from the surface of an NS at different directions is given by angle ζ (see Section 2.2.2). Different curves are calculated for different EoSs: APR (solid black), SLy4 (dotted blue), BSk24 (dashed red), and for the case of the strange star (dashed–dotted green). The upper and lower panels are given for NS mass 1.4 and 2 $M_\odot$, respectively.

more than an order of magnitude (see Fig. 7). Only at high energies $\sim$1 MeV, some fraction of neutrinos are absorbed, which reduce the flux directed towards a star (compare solid and dotted lines in Fig. 7).

4.3 Luminosity function

Using the calculated angular distributions of neutrino energy flux, we derive theoretical distributions of NSs over the neutrino amplification factor a_ν and calculate the fraction $\mathcal{F}(a_\nu)$ of NSs with amplification factors above specific values according to equation (25), as described in Section 3.2. These distributions are shown in Fig. 8.

One can see that the distributions of neutrino pulsars over the amplification factor are relatively restricted: the majority of objects exhibit amplification factors within the interval $a_\nu \in (0.5, 10)$. The anticipated population of objects with relatively large amplification factors decreases for larger NS masses (see Fig. 8). For the considered EoSs, only $\sim$0.1 per cent ($\sim$0.05 per cent) of neutrino pulsars demonstrate an amplification factor $a_\nu > 10$ for NS masses of 1.4 $M_\odot$ (2 $M_\odot$). The expected distribution of objects over the amplification factor depends on the EoS insignificantly (compare different lines in Fig. 8).

In the case of strange stars, the distribution of objects over the amplification factor depends on neutrino energy. About 10 per cent of ULX hosting strange stars can demonstrate amplification factor $a_\nu > 2$ and $\sim$0.01 per cent can show amplification factors $a_\nu > 10$ (see Fig. 9).

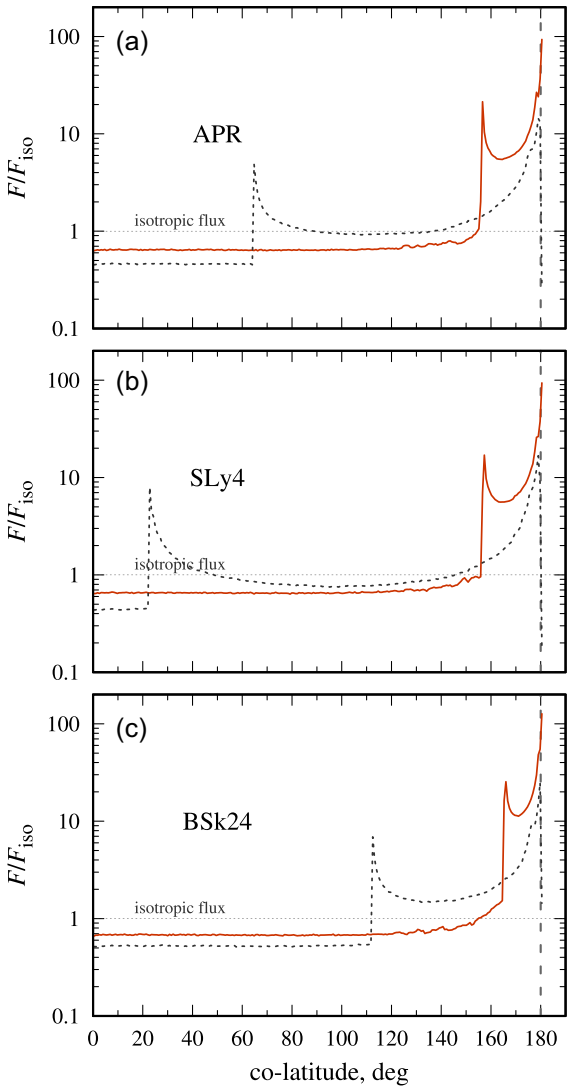

Figure 6. Angular distribution of neutrino energy flux from one of the poles of an NS is given by a red solid (black dotted) line for 1.4 $M_\odot$ (2 $M_\odot$) NS. The horizontal dotted line shows the level of the isotropic neutrino energy flux. Different panels correspond to different EoSs: (a) ARP, (b) SLy4, and (c) BSk24. In the case of relatively cold NSs under consideration, neutrino energy does not affect neutrino transfer within a star and, thus, the angular distribution.

5 SUMMARY

We have explored the impact of gravitational bending on neutrino emission in strongly magnetized NSs undergoing extreme mass accretion rates, such as bright X-ray transients or ULX pulsars. NS interiors in the considered class of objects are cold enough (temperature $\lesssim$10 keV) to be completely transparent to neutrino emission in keV and MeV energy bands (Haensel & Jerzak 1987). Thus, a fraction of neutrino emission is going through an NS experiencing gravitational bending. Through Monte Carlo simulations in the metric generated by spherically symmetric and quasi-static mass distribution within an NS, we simulated neutrino beam patterns (Figs 6 and 7) influenced by neutrino gravitational bending. The gravitational bending induces strong anisotropy in neutrino emission within the NS reference frame, leading to the phenomenon of neutrino pulsars.

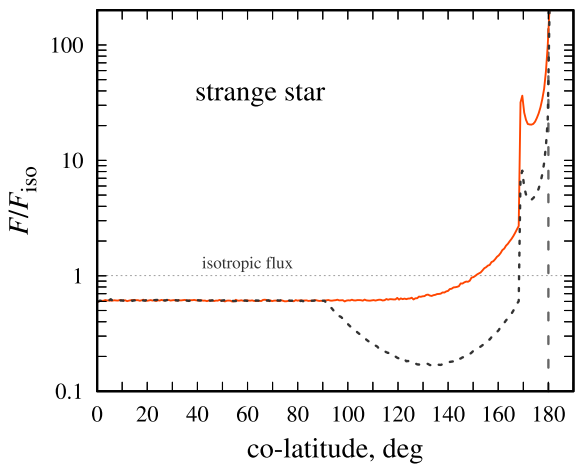

Figure 7. The angular distribution of neutrino energy flux from one of the poles of a strange star with $M = 1.4\,{\rm M}_\odot$ and M_r conforming with the EoS proposed by Zdunik (2000). Different lines are calculated for different neutrino energy: 100 keV (solid red) and 1 MeV (dotted black).

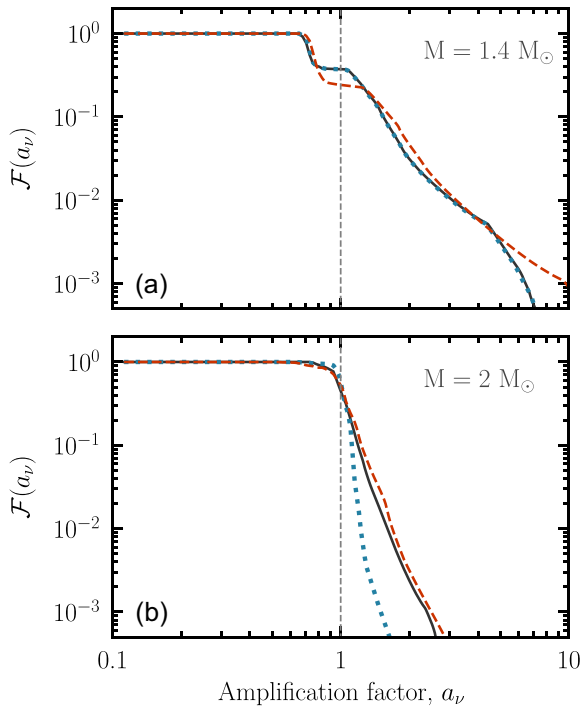

Figure 8. Fraction of neutrino pulsars of amplification factor exceeding a_ν. Different lines show results calculated for different EoSs: APR (solid black), SLy4 (dotted blue), and BSk24 (dashed red). Different panels correspond to different masses of an NS: (a) $M = 1.4\,{\rm M}_\odot$ and (b) $M = 2\,{\rm M}_\odot$. One can see that a large mass of an NS reduces significantly a fraction of strongly amplified sources.

Using calculated beam patterns, we have obtained the theoretical distributions of neutrino pulsars over the amplification factors (equation 1) that show the ratio of apparent (equation 17) and actual luminosity in neutrinos (see Figs 8 and 9). These distributions reveal limited ranges of amplification factors. The majority of neutrino pulsars are expected to fall within the interval $a_\nu \in (0.5, 10)$. For the considered EoSs, only approximately ∼0.1 per cent (∼0.05 per cent)

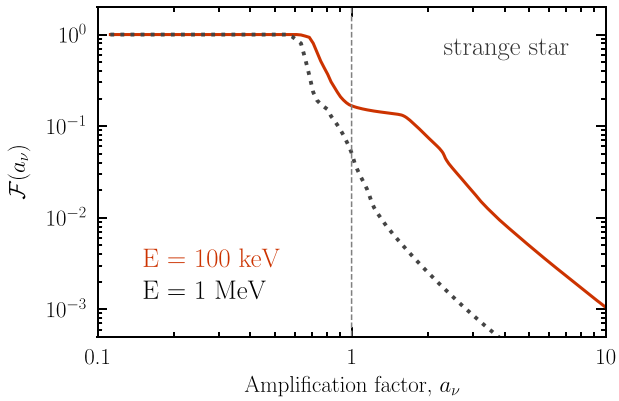

Figure 9. Fraction of neutrino pulsars of amplification factor exceeding a_ν calculated for the case of a strange star with $M = 1.4\,{\rm M}_\odot$ and M_r conforming with the EoS proposed by Zdunik (2000). Different lines are calculated for different neutrino energies: 100 keV (solid red) and 1 MeV (dotted black). The line corresponding to higher neutrino energy shows smaller fractions because of neutrino absorption in a star.

of neutrino pulsars exhibit an amplification factor $a_\nu > 10$ at an NS mass of $1.4\,{\rm M}_\odot$ ($2\,{\rm M}_\odot$). Thus, the expected neutrino flux from known pulsating ULXs and bright Be X-ray transients most likely remain below the isotropic neutrino background even in the case of flux amplification due to neutrino gravitational bending (see previous estimations that neglect gravitational bending in Asthana et al. 2023).

In the case of strange stars, where the core of a star is composed of quark matter, high-energy neutrinos can be subject to absorption. As a result, the neutrino beam pattern becomes energy dependent (see Fig. 7), which affects the expected distribution of objects powered by accretion onto strange start over the amplification factor (see Fig. 9). Note that presence of quark matter inside a star can cause some additional heating of the stellar interiors by the source of neutrino emission of the surface due to the neutrino absorption in such matter.

ACKNOWLEDGEMENTS

The authors thank Simon Portegies Zwart for the discussions. We are grateful to an anonymous referee for their useful comments and suggestions that helped us fix a mistake in the original version of the manuscript and improve the paper. AAM thanks UKRI Stephen Hawking fellowship. The work of AYP and IDM was partially supported by the Ministry of Science and Higher Education of the Russian Federation (agreement no. 075-15-2024-647).

DATA AVAILABILITY

The calculations presented in this paper were performed using a private code developed and owned by the corresponding author. All the data appearing in the figures are available upon request.

REFERENCES

Akmal A., Pandharipande V. R., Ravenhall D. G., 1998, Phys. Rev. C, 58, 1804
Alcock C., Farhi E., Olinto A., 1986, ApJ, 310, 261
Antoniadis J. et al., 2013, Science, 340, 448
Arzoumanian Z. et al., 2018, ApJS, 235, 37
Asthana A., Mushtukov A. A., Dobrynina A. A., Ognev I. S., 2023, MNRAS, 522, 3405

Bachetti M. et al., 2014, Nature, 514, 202
Basko M. M., Sunyaev R. A., 1975, A&A, 42, 311
Beloborodov A. M., 2002, ApJ, 566, L85
Blinnikov S., Yudin A., Kramarev N., Potashov M., 2022, Particles, 5, 198
Choudhury D. et al., 2024, ApJ, 971, L20
Doroshenko V. et al., 2022, Nat. Astron., 6, 1433
Doroshenko V. et al., 2023, A&A, 677, A57
Douchin F., Haensel P., 2001, A&A, 380, 151
Fabrika S. N., Atapin K. E., Vinokurov A. S., Sholukhova O. N., 2021, Astrophys. Bull., 76, 6
Fonseca E. et al., 2021, ApJ, 915, L12
Forsblom S. V. et al., 2024, A&A, 691, A216
Haensel P., Jerzak A. J., 1987, A&A, 179, 127
Haensel P., Potekhin A. Y., 2004, A&A, 428, 191
Haensel P., Zdunik J. L., Schaefer R., 1986, A&A, 160, 121
Haensel P., Potekhin A. Y., Yakovlev D. G., 2007, Neutron Stars 1: Equation of State and Structure. Springer, New York
Harding A. K., Lai D., 2006, Rep. Prog. Phys., 69, 2631
Heyl J. et al., 2024, Nat. Astron, 8, 1047
Horowitz C. J., Piekarewicz J., Reed B., 2020, Phys. Rev. C, 102, 044321
Israel G. L. et al., 2017, Science, 355, 817
Iwamoto N., 1982, Ann. Phys., 141, 1
Kaminker A. D., Levenfish K. P., Yakovlev D. G., Amsterdamski P., Haensel P., 1992, Phys. Rev. D, 46, 3256
King A., Lasota J.-P., Kluźniak W., 2017, MNRAS, 468, L59
Kraus U., 2001, ApJ, 563, 289
Lasota J.-P., King A., 2023, MNRAS, 526, 2506
Lindquist R. W., 1966, Ann. Phys., 37, 487
Malacaria C. et al., 2023, A&A, 675, A29
Markozov I. D., Mushtukov A. A., 2024, MNRAS, 527, 5374
Mihalas D., Mihalas B. W., 1985, Foundations of Radiation Hydrodynamics. Oxford Univ. Press, Oxford
Miller M. C. et al., 2019, ApJ, 887, L24
Misner C. W., Thorne K. S., Wheeler J. A., 1973, Gravitation. Freeman & Co., New York
Mönkkönen J., Tsygankov S. S., Mushtukov A. A., Doroshenko V., Suleimanov V. F., Poutanen J., 2022, MNRAS, 515, 571
Mushtukov A. A., Portegies Zwart S., 2023, MNRAS, 518, 5457
Mushtukov A. A., Tsygankov S., 2022, preprint (arXiv:2204.14185)
Mushtukov A. A., Suleimanov V. F., Tsygankov S. S., Poutanen J., 2015, MNRAS, 454, 2539
Mushtukov A. A., Verhagen P. A., Tsygankov S. S., van der Klis M., Lutovinov A. A., Larchenkova T. I., 2018a, MNRAS, 474, 5425
Mushtukov A. A., Tsygankov S. S., Suleimanov V. F., Poutanen J., 2018b, MNRAS, 476, 2867
Mushtukov A. A., Ognev I. S., Nagirner D. I., 2019, MNRAS, 485, L131
Mushtukov A. A., Portegies Zwart S., Tsygankov S. S., Nagirner D. I., Poutanen J., 2021, MNRAS, 501, 2424
Mushtukov A. A. et al., 2023, MNRAS, 524, 2004
Mushtukov A. A., Weng A., Tsygankov S. S., Mereminskiy I. A., 2024, MNRAS, 530, 3051
Nättilä J., Miller M. C., Steiner A. W., Kajava J. J. E., Suleimanov V. F., Poutanen J., 2017, A&A, 608, A31
Pal K., Dutt-Mazumder A. K., 2011, Phys. Rev. D, 84, 034004
Pearson J. M., Chamel N., Potekhin A. Y., Fantina A. F., Ducoin C., Dutta A. K., Goriely S., 2018, MNRAS, 481, 2994
Postnov K., Shakura N., Staubert R., Kochetkova A., Klochkov D., Wilms J., 2013, MNRAS, 435, 1147
Potekhin A. Y., Chabrier G., 2018, A&A, 609, A74
Potekhin A. Y., Zyuzin D. A., Yakovlev D. G., Beznogov M. V., Shibanov Y. A., 2020, MNRAS, 496, 5052
Reig P., 2011, Ap&SS, 332, 1
Rezzolla L., Most E. R., Weih L. R., 2018, ApJ, 852, L25
Richardson M. B., van Horn H. M., Savedoff M. P., 1979, ApJS, 39, 29
Riffert H., Meszaros P., 1988, ApJ, 325, 207
Romani R. W., Kandel D., Filippenko A. V., Brink T. G., Zheng W., 2022, ApJ, 934, L17
Saffer A. et al., 2024, preprint (arXiv:2412.02850)
Salmi T. et al., 2024, ApJ, 974, 294
Sawyer R. F., Soni A., 1979, ApJ, 230, 859
Schäfer T., Schwenzer K., 2004, Phys. Rev. D, 70, 114037
Shapiro S. L., Teukolsky S. A., 1983, Black Holes, White Dwarfs, and Neutron Stars: The Physics of Compact Objects. Wiley, New York
Tanashkin A. S., Karpova A. V., Potekhin A. Y., Shibanov Y. A., Zyuzin D. A., 2022, MNRAS, 516, 13
Tsygankov S. S., Doroshenko V., Lutovinov A. A., Mushtukov A. A., Poutanen J., 2017, A&A, 605, A39
Tsygankov S. S. et al., 2022, ApJ, 941, L14
Tsygankov S. S. et al., 2023, A&A, 675, A48
Vinciguerra S. et al., 2024, ApJ, 961, 62
Wang Y. M., Frank J., 1981, A&A, 93, 255
Weinberg S., 1972, Gravitation and Cosmology: Principles and Applications of the General Theory of Relativity. Wiley, New York
Witten E., 1984, Phys. Rev. D, 30, 272
Yakovlev D. G., Gnedin O. Y., Gusakov M. E., Kaminker A. D., Levenfish K. P., Potekhin A. Y., 2005, Nucl. Phys. A, 752, 590
Zdunik J. L., 2000, A&A, 359, 311
Zhang L., Blaes O., Jiang Y.-F., 2022, MNRAS, 515, 4371

APPENDIX A: GEODESIC LINES

Equation(15) can be rewritten in a form appropriate for numerical integration as follows:

$$\frac{\mathrm{d}r}{\mathrm{d}\varphi} = \pm r^2 \left(\frac{1}{A(r)B(r)\,b^2} - \frac{1}{A(r)\,r^2} \right)^{1/2}. \tag{A1}$$

The numerical modelling of neutrino trajectories based on this first-order differential equation requires a correct choice of the sign on the right-hand side, as described in Appendix B. One can avoid this sign ambiguity by using the second-order equation

$$\frac{2A(r)}{r^4}\frac{\mathrm{d}^2 r}{\mathrm{d}\varphi^2} + \frac{1}{r^4}\left(\frac{\mathrm{d}A(r)}{\mathrm{d}r} - \frac{4A(r)}{r}\right)\left(\frac{\mathrm{d}r}{\mathrm{d}\varphi}\right)^2 - \frac{2}{r^3} + \frac{\mathrm{d}B(r)/\mathrm{d}r}{b^2 B^2(r)} = 0, \tag{A2}$$

which is obtained by taking the derivative of both sides of equation (15) over r.

Based on the appendix in Beloborodov (2002), we can express b in terms of the trajectory variables. The tangent vector for the null geodesic line associated with the trajectory in the metric (equation 2) can be written as

$$u^\mu = \frac{\mathrm{d}x^\mu}{\mathrm{d}\lambda}, \tag{A3}$$

where μ is the index of the coordinate (t, r, θ, φ) and λ is an affine parameter. We can put $\theta = \pi/2$ without loss of generality. Killing vectors $\partial/\partial t$ and $\partial/\partial\varphi$ for equation (2) correspond to the integrals of motion u_t and $u_\varphi = b$, respectively. If we put $\lambda = 1/B(r)$, we get $u_t = -1$. Then from the condition $u^\mu u_\mu = 0$ we obtain

$$(u^r)^2 = \frac{1}{A(r)B(r)} - \frac{b^2}{A(r)\,r^2}. \tag{A4}$$

Let us consider the massless particle at the radius r and denote the angle between the particle momentum and the radial vector from the centre of symmetry as ζ. Then

$$\tan\zeta = \left(\frac{u^\varphi u_\varphi}{u^r u_r}\right)^{1/2} = \frac{b}{r}\left(\frac{1}{B(r)} - \frac{b^2}{r^2}\right)^{-1/2}. \tag{A5}$$

Therefore, b can be related to r and ζ as follows:

$$\sin\zeta = \frac{b}{r}\sqrt{B(r)}. \tag{A6}$$

Since the vector fields $\partial/\partial t$ and $\partial/\partial\varphi$ are the Killing fields both for the Schwarzschild metric and equation (2), the value of b does not change if the particle crosses the NS surface. Thus we arrive at equation (16).

Let us consider opacity transformation in general relativity. The neutrino transport process can be described by the relativistic Boltzmann equation for massless particles that can be written as (Lindquist 1966)

$$k^\alpha \frac{\partial \mathcal{I}}{\partial x^\alpha} - \Gamma^\alpha_{\beta\gamma} k^\beta k^\gamma \frac{\partial \mathcal{I}}{\partial k^\alpha} = \mathcal{J} - \kappa \mathcal{I}. \tag{A7}$$

Here, $\Gamma^\alpha_{\beta\gamma}$ are the Christoffel symbols, k^α is the particle four-momentum, and $\mathcal{I} = I_\nu(\Omega)/\nu^3$ is the invariant specific intensity. The ordinary specific intensity $I_\nu(\Omega)$ is usually defined in relation to the radiative transfer (e.g. Mihalas & Mihalas 1985), where ν is the photon frequency and Ω is the photon propagation direction. Note that in general relativity the photon frequency can be defined only in the local rest frame associated with an observer. In our case, the frequency is $\nu = \hat{k^0}/h$, where h is the Planck constant and k^0 is the neutrino energy measured in the reference frame of the observer whose (r, θ, φ) coordinates do not change. Since $\partial/\partial t$ is the Killing vector for the spherical static metric (equation 2), $\nu\sqrt{B(r)} =$ constant.

Furthermore, $\mathcal{J} = j_\nu/\nu^2$ in equation (A7) is an invariant emissivity, j_ν being an ordinary emissivity; $\kappa = \nu\alpha_\nu$ is an invariant absorption coefficient, $\alpha_\nu \propto 1/\lambda_\nu$, being an ordinary absorption coefficient, and λ_ν is a mean free path at the frequency ν. The quantities j_ν, α_ν, and λ_ν are defined in the same reference frame as the frequency ν. For an accurate calculation of neutrino transfer in NSs, it is necessary to take into account the transformation of the mean free path along the geodesic line due to the change of the metric coefficient $B(r)$. Since the typical mean free path of a neutrino with energy of a few hundred keV is very large in comparison with the typical NS radius (see Section 2.2.1), we can neglect neutrino opacities in the NSs. In the quark stars, we can neglect neutrino scattering, but should take into account neutrino absorption.

In our numerical model, we trace the motion of each neutrino as it propagates through an NS. Let us consider a neutrino moving from $(t, r, \pi/2, \varphi)$ to $(t + \mathrm{d}t, r + \mathrm{d}r, \pi/2, \varphi + \mathrm{d}\varphi)$ in Schwarzschild coordinates (t, r, θ, φ) (without loss of generality, we assume $\theta = \pi/2 =$ const). The spatial displacement vector $\boldsymbol{\delta l} = (\mathrm{d}r, 0, \mathrm{d}\varphi)$ lies in the tangent space at the point $(t, r, \pi/2, \varphi)$ and is represented in the coordinate basis as

$$\boldsymbol{\delta l} = \mathrm{d}r \frac{\partial}{\partial r} + \mathrm{d}\varphi \frac{\partial}{\partial \varphi}. \tag{A8}$$

The optical depth $\mathrm{d}\tau$ associated with this infinitesimal displacement $\boldsymbol{\delta l}$ is $\mathrm{d}\tau = \mathrm{d}\bar{s}/\lambda$, where λ is the neutrino mean free path and $\mathrm{d}\bar{s}$ is the length of the spatial motion. Both quantities are evaluated in the local Minkowski frame corresponding to the element of matter with which the neutrino interacts.

We assume the NS matter is at rest; therefore, the local orthonormal basis is

$$\begin{aligned} \boldsymbol{e}_{(0)} &= \frac{1}{\sqrt{B(r)}}\frac{\partial}{\partial t}, \quad \boldsymbol{e}_{(1)} = \frac{1}{\sqrt{A(r)}}\frac{\partial}{\partial r}, \\ \boldsymbol{e}_{(2)} &= \frac{1}{\sqrt{r}}\frac{\partial}{\partial \theta}, \quad \boldsymbol{e}_{(3)} = \frac{1}{\sqrt{r\sin^2(\theta)}}\frac{\partial}{\partial \varphi}. \end{aligned} \tag{A9}$$

In this basis, the displacement vector is

$$\boldsymbol{\delta l} = \sqrt{A(r)}\,\mathrm{d}r\,\boldsymbol{e}_{(1)} + r\,\mathrm{d}\varphi\,\boldsymbol{e}_{(3)}.$$

Its length is

$$\mathrm{d}\bar{s} = \sqrt{A(r)(\mathrm{d}r)^2 + r^2(\mathrm{d}\varphi)^2}. \tag{A10}$$

Note that $\mathrm{d}\bar{s}$ is numerically identical to the length computed in the spatial part of the spherically symmetric metric (equation 2), because $\boldsymbol{e}_{(0)}$ is parallel to $\partial/\partial t$, as the NS matter is at rest.

The mean free path depends on the neutrino energy, which changes along the geodesic due to gravitational redshift:

$$E_\nu \propto 1/\sqrt{B(r)}. \tag{A11}$$

This effect is fully accounted for in our Monte Carlo modelling.

APPENDIX B: SIMULATIONS OF NEUTRINO TRAJECTORIES

We calculate neutrino trajectories, described by differential equation (15), where the mass distribution is spherically symmetric and given by M_r. The impact factor can be calculated from the initial direction of particle motion according to equation (16). A trajectory is determined by the initial coordinates of a particle $\boldsymbol{r}_0$ and initial direction of its motion, which is given by the unit vector of particle velocity:

$$\boldsymbol{e}_{v0} = \frac{\boldsymbol{v}_0}{|\boldsymbol{v}_0|}. \tag{B1}$$

Simulating a trajectory, we choose a spatial separation between the nearest two points of approximate trajectory Δs and follow the steps:

(i) Using the starting point of particle trajectory $\boldsymbol{r}_0$ and the direction of its initial velocity given by the unit vector $\boldsymbol{e}_{v0}$ (equation B1), we calculate the second point of approximate trajectory:

$$\boldsymbol{r}_1 = \boldsymbol{r}_0 + \boldsymbol{e}_{v0}\Delta s. \tag{B2}$$

At this step $i = 1$.

(ii) Then we get the angle between positions $\boldsymbol{r}_i$ and $\boldsymbol{r}_{i-1}$:

$$\cos\Delta\varphi_{i,i-1} = \frac{(\boldsymbol{r}_i, \boldsymbol{r}_{i-1})}{|\boldsymbol{r}_i|\,|\boldsymbol{r}_{i-1}|}, \tag{B3}$$

where $(\boldsymbol{r}_i, \boldsymbol{r}_{i-1}) = \sum_{j=1}^{3} r_i^{(j)} r_{i-1}^{(j)}$ denotes the scalar productions of two vectors and $r_i^{(j)}$ is jth Cartesian coordinate of vector $\boldsymbol{r}_i$.

(iii) We get direction towards the $(i+1)$th point of approximate particle trajectory:

$$\boldsymbol{e}_{r,i+1} = \frac{\boldsymbol{r}_i + \boldsymbol{e}_{v,i-1}\Delta s}{|\boldsymbol{r}_i + \boldsymbol{e}_{v,i-1}\Delta s|}, \tag{B4}$$

and the angle between $\boldsymbol{e}_{r,i+1}$ and $\boldsymbol{r}_i$:

$$\Delta\varphi^*_{i+1,i} = \frac{(\boldsymbol{e}_{r,i+1}, \boldsymbol{r}_i)}{|\boldsymbol{r}_i|}. \tag{B5}$$

(iv) Using the second-order Runge–Kutta method, applied to the differential equation (A1), we compute the radial distance r_{i+1} at the next step of the simulation. The sign on the right-hand side of equation (A1) is determined based on whether the particle is moving towards or away from the centre of the star. If the right-hand side of equation (A1) becomes zero at any step, the sign changes in the next step. This corresponds to the particle reaching its minimum distance from the centre for a given impact parameter b.

(v) We get an estimation of the radial distance towards a new point of particle trajectory $r_{i+1} \simeq 0.5R_{\rm Sch}(M_i)/u_{i+1}$ and calculate its position:

$$\boldsymbol{r}^*_{i+1} = r_{i+1}\boldsymbol{e}_{r,i+1}. \tag{B6}$$

(vi) Because we want to get trajectory approximated by segments of a fixed length Δs, we recalculate the position of the latest point of neutrino trajectory as

$$\boldsymbol{r}_{i+1} = \boldsymbol{r}_i + \frac{\boldsymbol{r}^*_{i+1} - \boldsymbol{r}_i}{|\boldsymbol{r}^*_{i+1} - \boldsymbol{r}_i|}\Delta s. \tag{B7}$$

The unit vector of neutrino velocity at the latest segment of trajectory is given by

$$\boldsymbol{e}_{v,i} = \frac{\boldsymbol{r}_{i+1} - \boldsymbol{r}_i}{|\boldsymbol{r}_{i+1} - \boldsymbol{r}_i|}. \tag{B8}$$

(vii) We stop trajectory simulation if the particle experiences scattering at a given coordinate or if it is far from the central compact object: $|\boldsymbol{r}_{i+1}| > 5 \times 10^2 R_{\rm Sch}$. In this case, we have a final direction of particle motion given by equation (B8). Otherwise, we return to step (iii) and continue the simulation of the trajectory.

To control the accuracy of trajectory calculations, we perform it for smaller spatial step $\Delta s_1 = 0.5\,\Delta s$. In the case of similar results of the simulation, we stop the improvement of accuracy.

The results of the performed algorithm outside an NS were verified by comparison of its results with the results of algorithms applied earlier by Mushtukov et al. (2018a, 2024) to trace photon trajectories in XRPs.

This paper has been typeset from a TEX/LATEX file prepared by the author.